nature communications

Article

https://doi.org/10.1038/s41467-025-66937-9

# A nanofluidic oscillating neuron

Received: 23 April 2025

Accepted: 18 November 2025

Published online: 07 December 2025

Check for updates

Tianyi Xiong[1,2], Xiulan He[3], Boyang Xie[1,2], Guangguo Guo[1], Yueru Zhao[1,2], Ying Liu[1,2], Cong Pan[1], Yanan Jiang[3], Wenjie Ma[1], Fei Wu[3], Ping Yu[1,2] & Lanqun Mao[3]

Nanofluidics provide a transformative platform for creating neuron emulates, yet replicating their complex spiking dynamics remains challenging. Herein, we report a nanofluidic oscillating neuron (FON) which could emulate spiking-form encoding functions of neurons. This device showed neuromorphic oscillating ion conductance with a polyimidazolium-confined nanofluidic system in asymmetric solution environment. Similar with neuronal action potentials, the spiking originates from the anion/cation selectivity changes of polyimidazolium channels due to the dynamic interplay between the desorption/adsorption of $Fe(CN)_6^{3-}$ and the corresponding change of electroosmotic flow. The FON could emulate neuronal electrical and chemical encoding with diverse and controllable spiking patterns. More importantly, the refractory-period-like threshold changes of neuron could also be successful accomplished. This study demonstrated the potential of nanofluidic iontronics by rationally controlling the ion dynamics for neuromorphic computing and biomimetic device with diverse functions.

Nanofluidics mimicking the architecture and functions of neural systems have demonstrated transformative potential in multidisciplinary fields[1] including energy harvesting[2–4], intelligent sensing[5,6], biotic-abiotic interfacing[7] and fluidic computing[8–10]. For example, biomimetic nanofluidic ion channels like ionic diodes[11], ionic transistors[12] and ionic switches[13] have shown great potential in ionic sieving[14], ultrafast permeation[15] and signal amplification[16], closely mirroring the structure and functions of their biological counterparts. Recently, nanofluidic memristors emulating synapses have demonstrated multifarious neuromorphic functions including neuroplasticity[17], signal transduction[18], fluidic logic[19] and brain-inspired computing[20]. These nanofluidic devices highlighted the inherent computing power of nanofluidics, wherein neuron-like intelligent processing of both electrical signals and chemical signals was achievable through confined ion dynamics[21,22]. In this case, neuromorphic nanofluidics emulating the active potential behaviors are critically required. This would not only introduce an efficient spike-form processing paradigm to nanofluidic computing systems but also establish biotic-abiotic communication with ionic spikes.

However, nanofluidic neuron analog has long been in theoretical prediction, primarily due to the inherently complex nonlinear kinetics of neural spikes[23]. Attempts on solid-state neurons[24–26] and electrochemical neurons[27–29] have shown that action potential emulating was accessible by replicating neuronal spiking principles with integrated devices. Additionally, nanofluidic models proposed by Bocquet et al.[30] and Roij et al.[31] predicted that spiking ion current could be accomplished using nanofluidic memristor circuitry by mimicking ion transport kinetics of $K^+$ and $Na^+$ channels. Bisquert et al.[32] established a minimal neuron model utilizing a single nanofluidic device. These studies underscore the feasibility of emulating the neural spikes with nanofluidics. Furthermore, experimental attempts on ion current oscillation indicated that nonlinear ion transport is accessible in nanofluidics by tuning ion transport with nanoprecipitation[33], coherent resonance[34], chemical oscillation[35] and surface effects[36]. Nevertheless, challenges in emulating sophisticated neural coding paradigms have been hindering the step toward practical nanofluidic neurons, as the creation and control of nanofluidic systems with multiple steady states remain a fundamental bottleneck.

[1]Beijing National Laboratory for Molecular Sciences, Key Laboratory of Analytical Chemistry for Living Biosystems, Institute of Chemistry, Chinese Academy of Sciences (CAS), Beijing, China. [2]University of Chinese Academy of Sciences, Beijing, China. [3]College of Chemistry, Beijing Normal University, Beijing, China. e-mail: yuping@iccas.ac.cn; lqmao@bnu.edu.cn

Herein, we present a nanofluidic oscillating neuron (FON) capable of emulating the oscillatory neural spiking behaviors and neural encoding mechanisms by mimicking the mechanism of biological neurons. In biological neurons, the recognition of extracellular transmitters regulates the alternating activation of influx $Na^+$ channels and efflux $K^+$ channels, generating spike-form ion current (Fig. 1A)[37]. Inspired by this mechanism, our FONs are fabricated using polyimidazolium brushes (PimB)-modified micropipettes in asymmetric solution—backfilled with a mixture of KCl and $K_3Fe(CN)_6$ solution and immersed in a pure KCl bath, mimicking ion channels operating under asymmetrically distributed transmitter conditions. By modulating surface chemistry changes via Pim-$Fe(CN)_6^{3-}$ recognition and following electroosmotic flow (EOF) changes, anions and cations alternatively governed FON operation, consequently leading to the neural-like oscillating current under constant biases (Fig. 1B), mimicking the alternative activation of $K^+$/$Na^+$ channels in biological neurons. Benefited from this biomimetic design principle, FON exhibits high controllability and diverse ion dynamics. Variations in the applied electric signal and chemical environment enable precise regulation of the oscillating signal patterns of FON, thereby allowing the emulation of neural encoding functions both for electrical and chemical signals. This programmability toward electrical and chemical information changes further contributed to the successful simulation of dynamic threshold modulation analogous to neuronal refractory states by tuning the asymmetric solution gradient. These results not only offered the possibility of establishing a spiking neural network with nanofluidics but also paved the way for intelligent chemical regulation of nanofluidic biointerfaces in spike-form signals.

## Results

### Oscillating ion current in FON

The FON device was fabricated using a micropipette functionalized with PimB via surface-initiated atomic transfer radical polymerization (SI-ATRP) (Supplementary Fig. 1A)[38–40]. Current-voltage (*I-V*) measurements in 10 mM KCl revealed typical ion current rectification (ICR)[38] and memristive behavior[18], confirming the successful modification of PimB (Supplementary Fig. 1C). Scanning electron microscopy (SEM) images of the micropipette before and after modification showed a tip diameter of 3 μm and a uniform PimB layer on the inner surface (Supplementary Fig. 2A, B). To establish the asymmetric solution environment, the PimB-modified micropipette was backfilled with 0.1 M KCl containing 1 mM $K_3Fe(CN)_6$ and immersed in a 0.1 M KCl bath. Electrical contact was made using home-made Ag/AgCl wires (Supplementary Fig. 1B). Upon application of a−3 V bias, an oscillating ion current with a period of 4.02 s was observed in the conductance-time (*G-t*) profile (red curve, Fig. 1C), which was consistent with the peak at 0.31 Hz in the power spectrum (red curve, Fig. 1D). In contrast, only conductance decay in the *G-t* curve was observed in symmetric 0.1 M KCl solution, and no detectable peak was observed in the power spectrum (blue curve, Fig. 1C, D)[33]. According to nanopore noise analysis theories, such sub-Hz power spectral signals are attributed to dynamic surface chemical processes[41,42], suggesting that the observed oscillations originate from surface interactions within the confinement. These results indicate that surface chemical changes, driven by the interaction between the backfilled $K_3Fe(CN)_6$ and the PimB, mediate the emergence of the oscillating current in the FON.

To validate the role of $Fe(CN)_6^{3-}$ in FON, *I-V* curves of the PimB-modified micropipettes were conducted in a symmetric solution of 100 mM KCl containing $K_3Fe(CN)_6$ with different concentrations. As shown in Fig. 2A, typical ICR behavior was observed for the PimB-modified micropipettes with low $Fe(CN)_6^{3-}$ concentration (e.g., w/o $Fe(CN)_6^{3-}$ or 0.1 mM $Fe(CN)_6^{3-}$), indicating the anion selectivity and the low ion conductance state at the negative potential (red and orange curves, Fig. 2A). With the increase of the $Fe(CN)_6^{3-}$ concentration (e.g., 1 or 5 mM $Fe(CN)_6^{3-}$), the ICR inversion was observed, accompanied by a transition of the ion current to a high conductance state under negative potential (blue and purple curves, Fig. 2A). In this case, the high

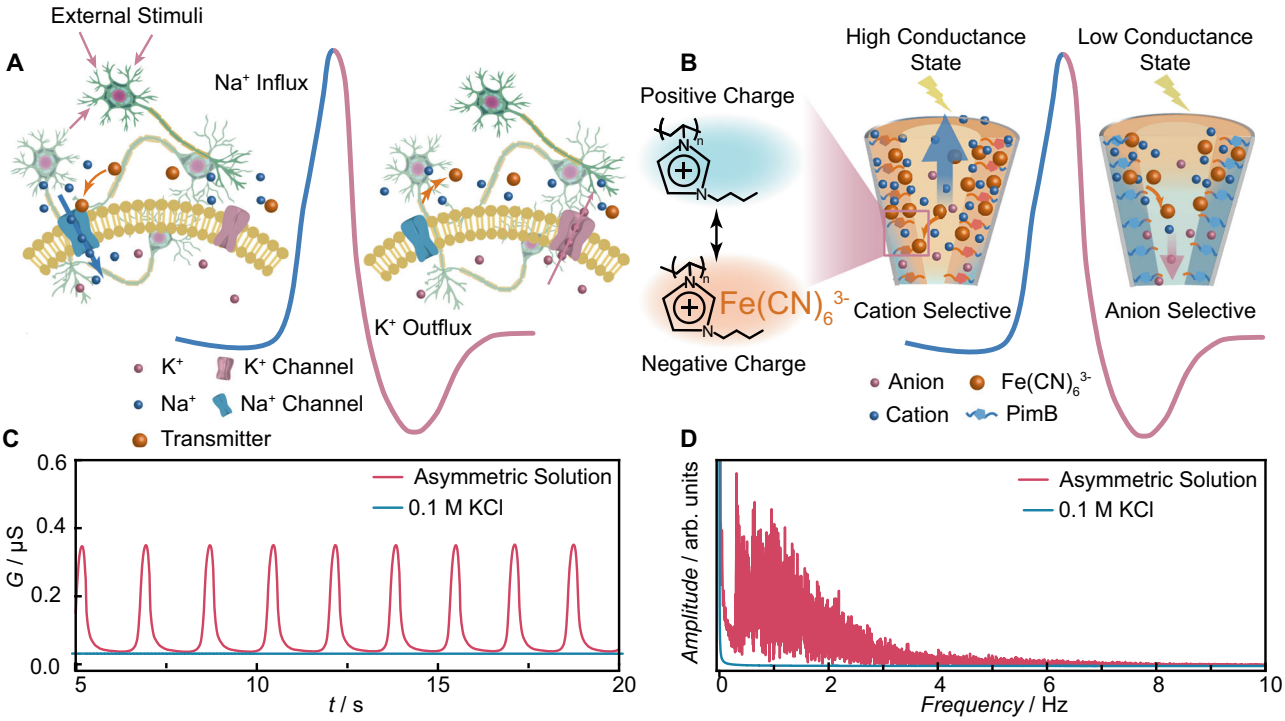


**Fig. 1 | Oscillating ion current spikes of FON.** Schematic illustration of the spiking mechanism of **A** biological neuron and **B** FON. **C** Plots of conductance versus time of a PimB-modified micropipette in asymmetric solution (inner: 0.1 M KCl+1 mM $K_3Fe(CN)_6$, outer: 0.1 M KCl; red curve) and 0.1 M KCl symmetric solution (blue curve) under −3 V bias. **D** Power spectra derived from (**C**).

https://doi.org/10.1038/s41467-025-66937-9

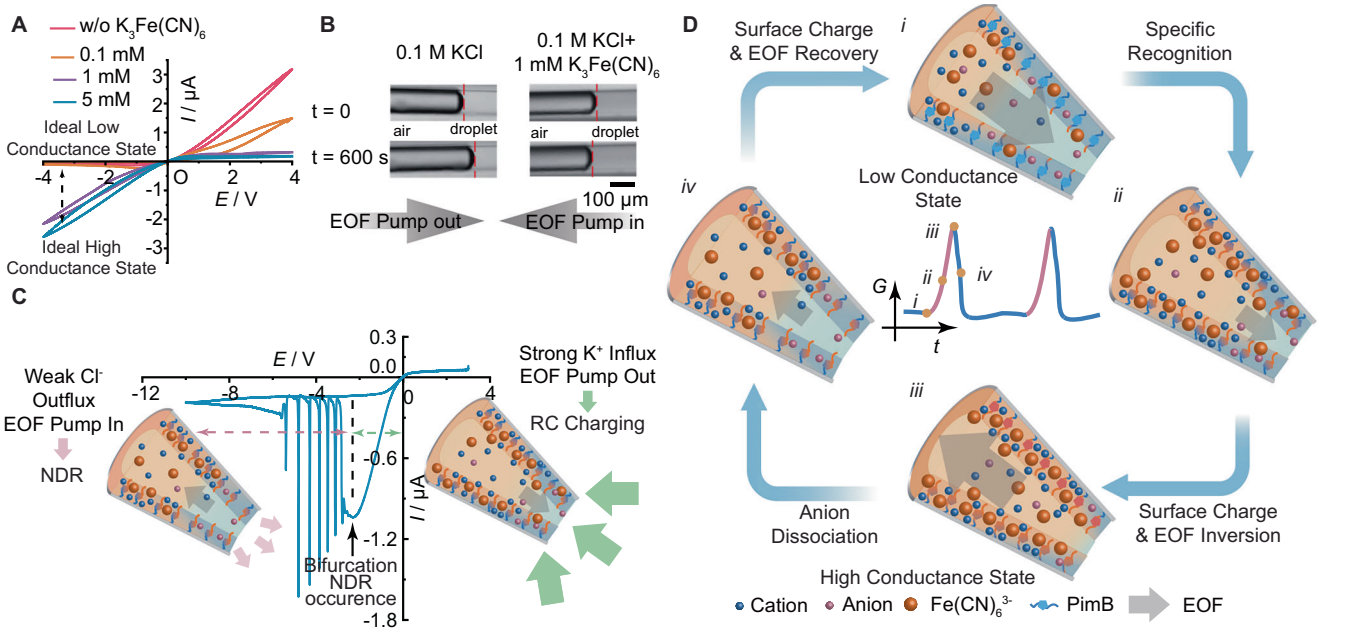


**Fig. 2 | Conductance state changing kinetics in FON. A** *I-V* curves of a PimB-modified micropipette in symmetric 0.1 M KCl containing $K_3Fe(CN)_6$ with different concentration, scan rate 50 mV·s$^{-1}$. **B** Optical microscopy image of air-droplet interface movement in a capillary connected with a PimB-modified micropipette in 0.1 M KCl (left) and 0.1 M KCl+1 mM $K_3Fe(CN)_6$ (right) under −3 V bias. **C** Typical *I-V* curve of a PimB-modified micropipette in asymmetric solution (inner, 0.1 M KCl +1 mM $K_3Fe(CN)_6$; outer, 0.1 M KCl), scan rate 50 mV·s$^{-1}$. Inset, schematic illustration of the $K^+$ governed RC process (right) and the $Cl^-$ governed NDR process (left). **D** Schematic illustration of the ion conductance changing mechanism of FON, (i) initial low conductance state with few Pim-$Fe(CN)_6^{3-}$ interaction in the PimB layer; (ii) Pim-$Fe(CN)_6^{3-}$ adsorption contributed to raising ion conductance under negative bias; (iii) High conductance state with the majority of PimB layer adsorbed by $Fe(CN)_6^{3-}$, inverted EOF pumped external KCl solution into FON; (iv) Desorption of $Fe(CN)_6^{3-}$ in KCl solution contributed to the recovered conductance and EOF in FON.

conductance state and low conductance state under negative potential could be regulated by the concentration of $Fe(CN)_6^{3-}$. Previous reports have shown strong ionic hydrogen-bond interactions between PimB and $Fe(CN)_6^{3-}$ (Supplementary Fig. 3, inset), which facilitates the over-adsorption of $Fe(CN)_6^{3-}$ on the PimB[43,44], and consequently results in the ICR inversion[45]. This surface charge inversion induced by specific PimB-$Fe(CN)_6^{3-}$ recognition was further corroborated by zeta potential measurements of PimB-modified $SiO_2$ nanoparticles (PimB-SiNPs) in 100 mM KCl containing $K_3Fe(CN)_6$ with different concentrations. Increasing the $Fe(CN)_6^{3-}$ concentration shifted the surface charge from positive to negative (Supplementary Fig. 3), confirming charge inversion mediated by Pim-$Fe(CN)_6^{3-}$ recognition. These results essentially demonstrated that the specific PimB-$Fe(CN)_6^{3-}$ recognition leads to a transition between high and low conductance states, mediated by the $Fe(CN)_6^{3-}$ concentration. Thus, in an asymmetric solution, changes in the localized $Fe(CN)_6^{3-}$ distribution could lead to switching between these two distinct conductance states. Analogous to biological neurons, FON generate ion current spikes through these recognition processes, highlighting their potential to mimic neuronal signaling kinetics.

Given that electrophoresis (EP) and EOF are two elemental factors governing confined ion transport[46,47], the influence of EOF on FON was further investigated. The orientation and velocity of EOF were quantified experimentally using EOF pump mechanism, which measured the movement of a dye droplet driven by EOF (Supplementary Note 1, Supplementary Fig. 4)[48]. As shown in Fig. 2C, upon application of a-3 V bias to the PimB-modified micropipette in 0.1 M KCl, a velocity of 19.0 ± 3.5 μm·s$^{-1}$ was observed by measuring the droplet movement distance, in which EOF drove the internal solution outward (left, Fig. 2B). Conversely, in 0.1 M KCl+1 mM $K_3Fe(CN)_6$ under the same bias, the inverted EOF pumped the external solution inward at a velocity of 3.2 ± 0.8 μm·s$^{-1}$ (right, Fig. 2B). These results indicate that surface chemistry changes induce changes in EOF orientation and velocity within FON. Notably, EOF exerts a strong influence on ion transport in asymmetric solution via localized changes in solution composition[20,49,50]. In the FON, surface-dependent EOF switching facilitates localized variations in solution content, thereby creating a feedback loop that modulates surface chemistry and enables conductance switching.

To further elucidate the EOF switching dynamics, finite element modeling (FEM) was conducted to simulate EOF variations. By introducing parameter $a$ describing the surface charge distribution changes induced by recognition level differences in the surface PimB layer, the EOF distribution under a-3 V bias was numerically solved using the Poisson-Nernst-Planck and modified Stokes-Brinkman equations (Supplementary Note 2 and Supplementary Fig. 5A). As the recognition level $a$ increased, the surface charge gradually inverted from positive to negative following a logistic distribution of charge density in PimB layer (Supplementary Fig. 6B), resulting in the inversion of EOF direction (Supplementary Fig. 6D) When the PimB layer was predominantly positively charged (e.g., $a = -0.05$, Supplementary Fig. 6B, C), EOF pumped the internal solution outward. With an increase in the recognition level, the majority charge in the PimB layer inverted to negative, causing EOF to drive the external solution into the micropipette gradually (e.g., $a = 0.3$, Supplementary Fig. 6A–C). This inversion of EOF indicates a coupling between surface chemistry and EOF: EOF regulates the localized $Fe(CN)_6^{3-}$ distribution in the asymmetric solution, which alters the surface charge; these surface chemical changes, in turn, control the orientation and velocity of EOF. This coupled interaction drives the ion conductance changes in the asymmetric solution, leading to the spiking phenomena of the FON.

To investigate the conductance changes associated with spiking dynamics, *I-V* curves of the FON in an asymmetric solution were further measured. First, changes of ion conductance states were revealed with *I-V* curves with narrowed potential window (−1 to 1 V) before and after the occurrence of spiking current. After applying a −3 V bias for 1 min

(which generated continuous spiking), the inverted ICR was observed (Supplementary Fig. 7), indicating a transition from a low to a high conductance state under negative bias due to surface charge inversion.

To directly observe the switching kinetics during the spiking phenomena, *I-V* curves were recorded under triangular waves with a wider potential window. As shown in Fig. 2C, FON in asymmetric solution (inner, 0.1 M KCl+1 mM $K_3Fe(CN)_6$; outer, 0.1 M KCl) showed negative differential resistance (NDR) at $E > -2$ V, followed by a bifurcation of the ion current—the spiking phenomenon. As the negative potential increased, an initial rise in ion current was observed, indicating a $K^+$ controlled high conductance state. A further increase in the negative potential led to NDR and bifurcation, suggesting that the FON switches to a $Cl^-$ controlled low conductance state under a strong negative potential. Notably, this NDR effect is induced by influx EOF, thus could be observed at higher negative potential only[51,52]. According to electrochemical oscillation theory, the alternating interplay between RC charging and NDR results in oscillating current. In the FON, $K^+$ transport is a RC charging process that increases ion conductance (left in Fig. 2C), while $Cl^-$ transport driven by EOF contributes to the NDR behavior, which drives the ion conductance reduction (right in Fig. 2C). The synergism between these two effects is thus responsible for the spiking phenomena.

Experimental and theoretical results indicate that the oscillating current spikes in FON originate from conductance state changes induced by the coupled interplay of EOF and surface chemistry. As depicted in Fig. 2D (state i), under a negative bias, $Cl^-$ initially serves as the predominant charge carrier within the positively charged PimB, resulting in a low conductance state. Concurrently, EOF pumps the inner $Fe(CN)_6^{3-}$ toward the orifice, enabling the $Fe(CN)_6^{3-}$ adsorption. The surface charge inversion resulting from the $Fe(CN)_6^{3-}$ adsorption shifts the dominant charge carrier to $K^+$, leading to an increase in ion conductance (Fig. 2D, state ii). This charge inversion not only causes the high conductance state but also reverses the EOF direction, driving external KCl solution into the micropipette (Fig. 2D, state iii). This influx promotes $Fe(CN)_6^{3-}$ desorption from PimB (Fig. 2D, state iv); the recovery of the original surface chemistry and EOF direction resets the system to the low conductance state. Consequently, the FON spontaneously switches between the $Cl^-$ dominated low conductance state and the $K^+$ dominated high conductance state, producing oscillating ion current spikes. Mirroring biological neurons, where action potentials emerge from alternating $K^+$ and $Na^+$ channel activity, the oscillating current in the FON stems from the alternating dominance of cation and anion conductance. This mechanism endows the FON with not only biomimetic fidelity but also unparalleled simplicity, enabling single-device emulation of neuronal spiking without auxiliary circuitry.

To give a quantitative understanding on the conductance change dynamics of FON, analysis on the ion conductance and force balance were carried out to establish the ion transport model within FON. Ion transport theories showed that ion conductance of FON is decided by the conductance of PimB layer, which is a monotonic function of charge density in the PimB layer under a constant bias. Force analysis on the $Fe(CN)_6^{3-}$ in FON showed that balance between inverted EOF and other driving forces contributed to two steady states under negative biases in asymmetric solution (Supplementary Note 3). Thus, by describing the ion current with variable $x$ and ion distribution states with variable $y$, the potential of the system could be described by a bistable well $U(x,y)$ (Supplementary Fig. 8A).

$$U(x,y) = \frac{1}{4}Ax^4 - \frac{1}{2}Bx^2 + Cxy \tag{1}$$

where $A$, $B$, and $C$ are descriptive coefficients for the bistable well, which is regulated by applied voltage as well as surface chemistry (Supplementary Note 3). Inspired by the ion current oscillation theories, we derived coupled state equations by assuming a simplified response of $y$[53],

$$\frac{dx}{dt} = Ax^3 - Bx + Cy \tag{2}$$

$$\frac{dy}{dt} = \gamma_y^{-1}\left[k^+H(x) - k^-H(L-x)\right] + D\xi(t) \tag{3}$$

Where $k^+$ and $k^-$ are the kinetic parameters related to recognition/dissociation processes, respectively, $H(x)$ is the Heaviside functions enforcing the adsorption/desorption kinetic, and $D$ is parameter for the stochastic disturbance $\xi(t)$ associated with the stochastic recognition processes. In this case, the spike-form oscillating current could be modeled by the numerical integration of Eq. 2 and Eq. 3 (Supplementary Fig. 8B), confirming the model's predictive power of the oscillating current. This simulation indicated that the bistable adsorption states induced by the interplay of surface chemistry and EOF led to the possibility of emulating spiking current with FON. Under an appropriate bias, EOF triggers surface chemistry transitions between the metastable states, contributed to oscillating ion current spikes. Therefore, by regulating the $Fe(CN)_6^{3-}$ transport kinetics, precise control on the spiking kinetics could be accessible, enabling possibility of emulating the current-spike-based encoding functions of neurons with FON.

## Neuromorphic spiking response of FON

Neurons transduce external stimuli into spike-form signals, encoding information through variations in event counts, frequency and timing[54,55]. Such dynamically reconfigurable spiking constitutes the biophysical basis of neural computation[23]. To validate this neuronal encoding function of FON, the voltage-gated spiking threshold was first characterized by applying a triangular wave to the FON device in asymmetric solution (inner: 0.1 M KCl+1 mM $K_3Fe(CN)_6$; outer: 0.1 M KCl). *I-V* curve indicated that spiking ion current occurs under negative bias. Critically, an all-or-none spiking behavior was observed, where spikes occur only when the bias exceeds a threshold value ($V_{th} = -2$ V), mimicking the excitability of biological neurons (Fig. 3A). This threshold phenomenon is consistent with the NDR observed in Fig. 2C, where intensive EOF under a strong bias voltage results in NDR and subsequent bifurcation. In contrast, *G-t* curve under a subthreshold bias (e.g., $V = -1$ $V < V_{th}$, Supplementary Fig. 9A) showed a current value rather than spikes, as insufficient bias cannot drive the switching kinetics of EOF and surface charge distribution. Meanwhile, *G-t* curves under positive biases exhibited a monotonic increase in conductivity due to the reversed directions of EOF (Supplementary Fig. 9B). This voltage-dependent threshold response quantitatively mirrors that of biological neurons, positioning FON as building blocks for neuromorphic circuits and enabling spike-based computing with nanofluidics.

To further validate the encoding function of FON, stimulus intensity-encoded spiking responses were demonstrated by systematically modulating the applied bias. As shown in Fig. 3B, *G-t* curves under different bias voltages revealed a stimulus-dependent spiking rate (electrolyte, inner: 0.1 M KCl+1 mM $K_3Fe(CN)_6$; outer: 0.1 M KCl), with the spiking frequency increasing from 2.1 ± 0.3 to 18.7 ± 1.2 Hz as the bias was raised from −2 to −5 V. This voltage-programmable frequency coding was corroborated by blue-shifted power spectra (from 2.4 to 19.1 Hz; Fig. 3C) and narrowing spike full-width-at-half-maxima (from 0.48 to 0.12 s; Fig. 3D). The increased applied bias enhances EOF velocity, thereby accelerating the transition kinetics between the high and low conductance states and leading to a higher spiking frequency. Concurrently, the increasing bias voltage also resulted in a damping of the conductance envelope under constant bias, as shown in Fig. 3B, which might be related to

https://doi.org/10.1038/s41467-025-66937-9

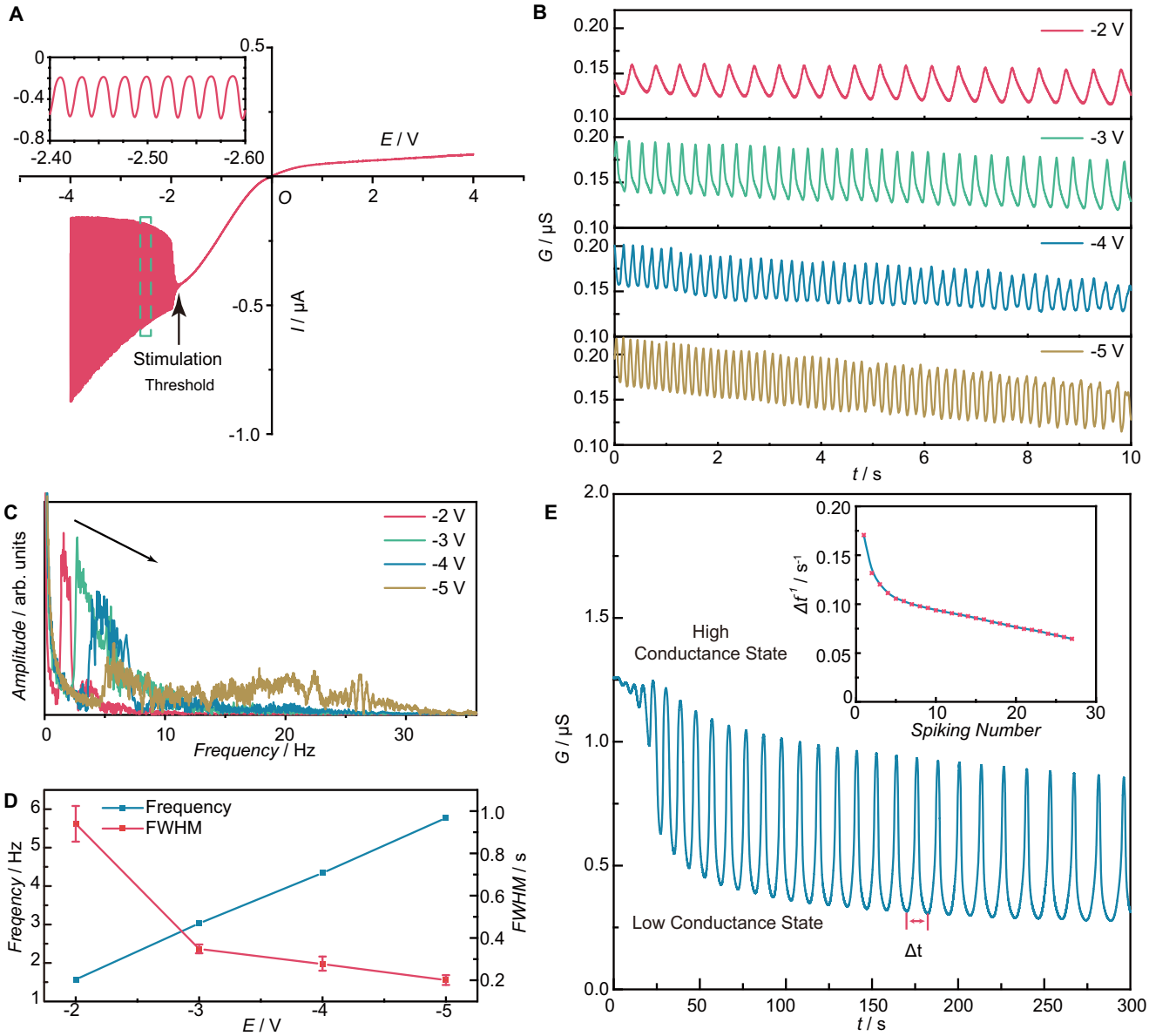


**Fig. 3 | Neuron-mimic spiking response of FON. A** *I-V* curve of a PimB-modified micropipette in asymmetric solution (inner: 0.1 M KCl+1 mM $K_3Fe(CN)_6$; outer: 0.1 M KCl), scan rate 50 mV·s$^{-1}$. Inset, zoom in the selected section. **B** Plots of conductance versus time of FON in asymmetric solution (inner: 0.1 M KCl+1 mM $K_3Fe(CN)_6$, outer: 0.1 M KCl) under different bias voltages. **C** Normalized power spectra derived from (**B**). **D** Plots of FWHM (red) and power spectra peak frequency (blue) versus bias voltage derived from (**B**) and (**C**), respectively. **E** *G-t* curve of a FON in asymmetric solution (inner: 0.1 M KCl+1 mM $K_3Fe(CN)_6$, outer: 0.1 M KCl) under a step voltage ($t < 0$, $E = 0$; $t \geq 0$, $E = -3$ V, the conductance under $E \leq 0$ was not recorded). Inset, the plot of localized frequency $\Delta t^{-1}$ versus spiking number.

the accumulation of $Fe(CN)_6^{3-}$ in the PimB layer, which reduced the ion conductance over time. Under a stronger bias, faster switching kinetics amplify this effect due to reduced dissociation time, resulting in not only faster spiking but also a more pronounced damping effect.

To theoretically elucidate the observed voltage-dependent ion current spikes, current responses under varying biases were simulated using the bistable model (Eqs. 2, 3). As the bias voltage directly modulates the energy barrier between steady states by controlling EOF in the FON, an increasing bias reduces this barrier, thereby inducing accelerated spiking behavior (Supplementary Fig. 10A, B). Conversely, insufficient or positive bias voltages trigger a transition of the bistable system to a steady state, where spiking ceases, and a monotonic current is observed instead (Supplementary Fig. 10C). These voltage-dependent spiking dynamics align with the Class I neuronal excitability of biological systems, wherein action potential generation requires stimulation surpassing a threshold current, and elevated stimulus intensity enhances spiking frequency[56]. This suggests that FON could emulate the core encoding mechanisms of neural dynamics, positioning these devices as promising candidates for nanofluidic computing circuits.

Beyond voltage-dependent encoding dynamics, the spike frequency adaptation (SFA) of biological neurons—a damping of frequency under sustained stimuli that maintains sensitivity to rapid stimuli[57], was emulated with FON to demonstrate their response kinetics. As shown in Fig. 3E, when a −3 V voltage step was applied, an initial burst of high-frequency spikes was observed, followed by a gradual frequency attenuation over time. This tendency was quantified by plotting the instantaneous frequency (described by the reciprocal period $\Delta t^{-1}$) over spiking number (Fig. 3E, inset). Similar to the damping conductance discussed earlier, the SFA characteristic of the device can be attributed to the incomplete dissociation of

https://doi.org/10.1038/s41467-025-66937-9

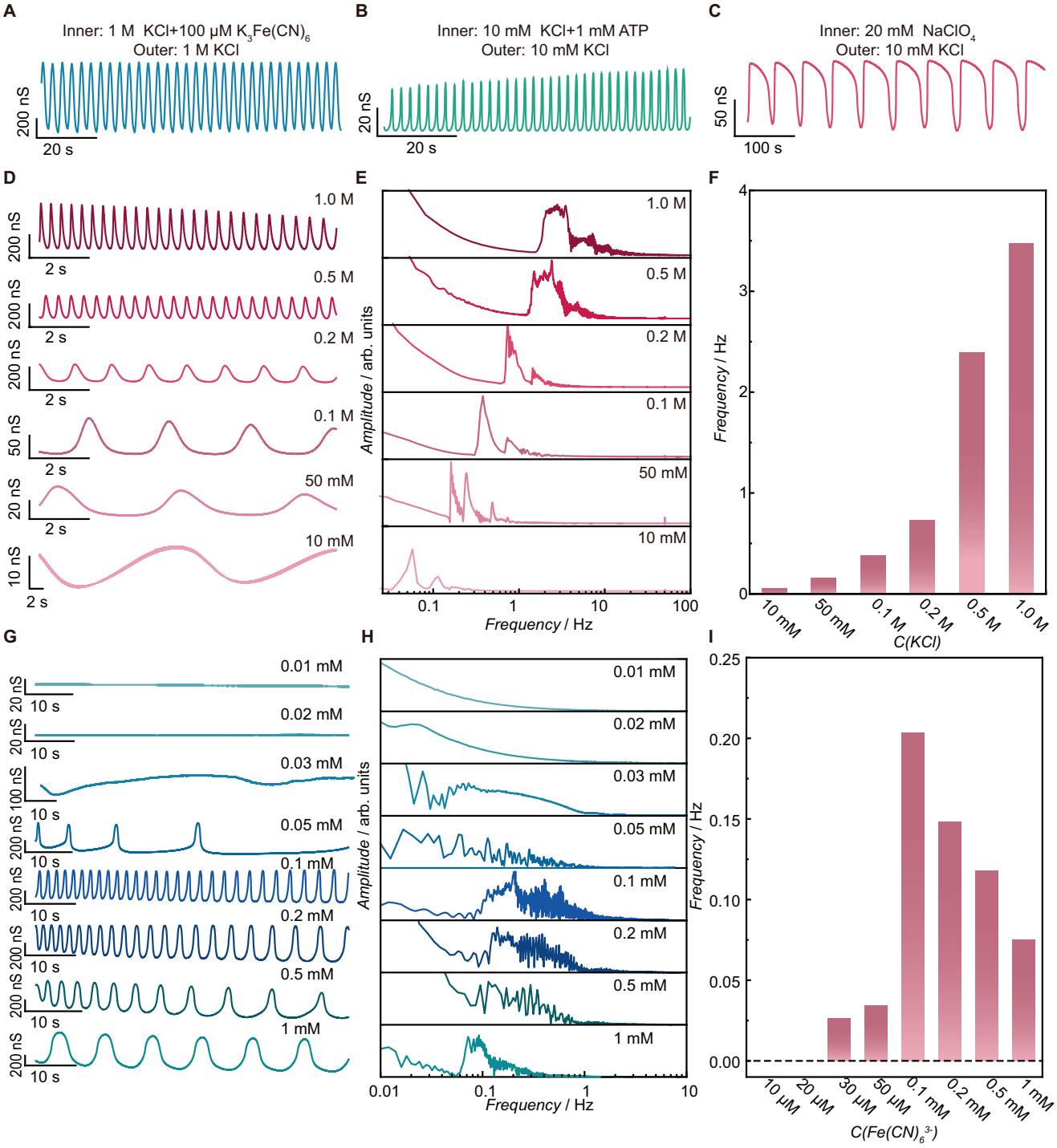


**Fig. 4 | Chemical regulated spiking of FON.** *G-t* curves of a FON with different asymmetric solution, **A** inner: 1 M KCl+100 μM $K_3Fe(CN)_6$; outer: 1 M KCl; **B** inner: 10 mM KCl+1 mM ATP; outer: 10 mM KCl; **C** inner: 20 mM $NaClO_4$; outer: 10 mM KCl; The applied bias was −3 V. **D** Typical *G-t* curves of a FON in asymmetric solution with different ionic strength (inner: 1 mM $K_3Fe(CN)_6$ + KCl with different concentration; outer: KCl with different concentration), bias voltage −3 V. **E** Power spectra derived from (**D**). **F** Plot of spiking frequency versus KCl concentration. **G** Typical *G-t* curves of a FON in asymmetric solution with different $K_3Fe(CN)_6$ concentration (inner: 0.1 M KCl + $K_3Fe(CN)_6$ with different concentration; outer: 0.1 M KCl), bias voltage −3 V. **H** Power spectra derived from (**G**). **I** Plot of spiking frequency versus $K_3Fe(CN)_6$ concentration.

$Fe(CN)_6^{3-}$. The accumulation of $Fe(CN)_6^{3-}$ modulates the EOF velocity, thereby altering the switching kinetics over time. This low-power encoding pattern presents opportunities for generating time-dependent spiking signals with nanofluidics, which is highly important for designing advanced neuromorphic computing systems.

## Chemical regulated spiking of FON

Beyond generating diverse current spike morphologies under electrical stimuli, FON simulated a core feature of biological neurons: the ability to transduce chemical signals into varying spiking currents. Toward emulating this chemical encoding capability, FON was first engineered by tuning the Pim-anion recognition intensity to show how

binding strength governs spiking behavior. As shown in Fig. 4A–C, changing the backfilled anion species under a fixed −3 V bias induced dramatic alterations in spiking dynamics. For $Fe(CN)_6^{3-}$, which has a high affinity for PimB as discussed, current spikes persisted even at low $Fe(CN)_6^{3-}$ concentrations and high ionic strength (e.g., inner: 1 M KCl +100 μM $K_3Fe(CN)_6$; outer: 1 M KCl), despite significant ionic shielding attenuating the recognition efficiency. In contrast, weaker ligands like ATP and $ClO_4^-$ (recognition intensity: $Fe(CN)_6^{3-}$ > ATP > $ClO_4^-$) require low ionic strength (e.g., 10 mM KCl) and elevated concentrations (e.g., 1 mM ATP or 20 mM $ClO_4^-$) to elicit spiking (Fig. 4B, C). Furthermore, the spiking frequency correlated with binding affinity, i.e. $f(Fe(CN)_6^{3-}) > f(ATP) >> f(ClO_4^-)$, which can be attributed to changes in the interfacial recognition-dissociation kinetics. This affinity-dependent modulation reveals opportunities to tune FON spiking dynamics through molecular design, enabling quantitative chemical manipulation over spiking signals.

To quantitatively assess the influence of Pim-anion interactions, we modulated the ionic strength within the system. Elevating the background KCl concentration from 0.01 to 1 M under −3 V bias (i.e., inner: 1 mM $K_3Fe(CN)_6$ + KCl with different concentration; outer: KCl with different concentration) resulted in accelerated spiking frequencies in the *G-t* curves (Fig. 4D), corresponding to blue shifts in the power spectra peaks (Fig. 4E, F). This observation indicates that by tuning the recognition/dissociation kinetics via ionic strength, precise spiking control can be realized in FON. Analogous to biological neurons, where ionic strength modulates action potential dynamics[56], the ionic strength dependence of FON enables the encoding of ionic environment information into spiking signal patterns.

Furthermore, the effect of ligand (i.e., $Fe(CN)_6^{3-}$) concentration on the spiking behaviors of FON was investigated to emulate the regulation dynamics of neurotransmitters. *G-t* curves in asymmetric solution with different $Fe(CN)_6^{3-}$ concentration (i.e., inner: 0.1 M KCl + $K_3Fe(CN)_6$ of different concentration, outer: 0.1 M KCl) under a −3 V bias were recorded. At low $Fe(CN)_6^{3-}$ concentrations, FON exhibited a $Fe(CN)_6^{3-}$ concentration-dependent threshold: spiking activity required a minimum of 30 μM $Fe(CN)_6^{3-}$, which produced low-frequency spiking at 21.8 mHz as shown in Fig. 4G (longer timescale were adopted for the derivation of power spectra to show the peak information and adopt the spiking frequency). The spiking frequency increased with rising $Fe(CN)_6^{3-}$ concentration, as proved by the blue shifts in the power spectra (Fig. 4H), reaching a maximum frequency at 0.1 mM $Fe(CN)_6^{3-}$. Notably, further increases of $Fe(CN)_6^{3-}$ concentration suppressed the spiking frequency (Fig. 4G, H), yielding a nonlinear concentration-response relationship (Fig. 4I). This biphasic behavior aligns with the nonlinear response kinetics of biological neurons, where a protective decrease of the response is observed under extreme stimuli. The stochastic resonance effect, stochastic disturbance-assisted enhancement of spiking signal, as widely observed in biological neuron[58,59], could theoretically explain this observation. By tuning the $Fe(CN)_6^{3-}$ dependent noise level in Eqs. 2 and 3, a resonant frequency maximum could be derived theoretically (Supplementary Fig. 11A–C). Remarkably, this nonlinear chemical response mimics neuronal adaptation to suprathreshold stimulation, highlighting the capacity of FON to implement neuron-mimic nonlinear encoding rules.

These chemical-mediated characteristics of FON demonstrate that by tuning PimB-anion interactions within nanoconfinement, chemical signals can be transduced into ion current spikes of varying patterns, thereby emulating the encoding mechanisms of neurons. These findings establish the feasibility of an iontronic computing paradigm in FON through programmable chemical regulation that mimics the transduction kinetics of biological neurons.

### Chemical regulated threshold of FON

To demonstrate the potential of neuron-mimic nanofluidic computing via chemically regulated spiking signals in FON, we emulated threshold modulation during the neuronal refractory period by regulating the internal concentration gradient. Following presynaptic transmitter stimuli, neurons enter a refractory state, becoming temporarily unresponsive to subsequent inputs to prevent overstimulation (Fig. 5A)[37], which is a fundamental chemically mediated spiking kinetics in neurons.

To replicate this chemical-mediated threshold switching in FON, we introduced $Fe(CN)_6^{3-}$ at varying concentrations into the external bath, thereby modulating the chemical gradient to mimic postsynaptic depolarization. In the absence of external $Fe(CN)_6^{3-}$, the FON exhibited a low threshold voltage of −2 V (inner: 0.1 M KCl+1 mM $K_3Fe(CN)_6$; outer: 0.1 M KCl), as shown in Fig. 3A. This configuration establishes a strong $Fe(CN)_6^{3-}$ concentration gradient, resulting in the low spiking threshold. Conversely, reducing this gradient by introducing $Fe(CN)_6^{3-}$ to the external bath increased the bias required to initiate spiking, mimicking the elevated threshold characteristic of refractory states (inner: 0.1 M KCl+1 mM $K_3Fe(CN)_6$; outer: 0.1 M KCl + 10 μM $K_3Fe(CN)_6$, Fig. 5B). Increases in the external $Fe(CN)_6^{3-}$ concentration induced threshold shifts (inner: 0.1 M KCl+1 mM $K_3Fe(CN)_6$; outer: 0.1 M KCl + 50 μM $K_3Fe(CN)_6$, Figure 5C), with 100 μM $Fe(CN)_6^{3-}$ establishing an absolute refractory state where spiking was abolished even under a −10 V stimulus (inner: 0.1 M KCl+1 mM $K_3Fe(CN)_6$; outer: 0.1 M KCl + 100 μM $K_3Fe(CN)_6$, Fig. 5D). These chemically induced threshold modulations underscore the capacity of FON to achieve reconfigurable spiking logic through programmable chemical environments.

Critically, the spiking behavior of FON arises from the interdependent $K^+$ governed NDR and $Cl^-$ governed RC charging process as discussed. In this case, both the electrical field and the concentration gradient regulated the occurrence of bifurcation by controlling the intensity of these 2 processes. With raise of external $Fe(CN)_6^{3-}$ concentration, changes in charge density distribution resulted in regulation of EOF velocity in FON, resulting in stronger voltage requirement for the occurrence of spiking behavior, which contributed to the threshold shifts of the device (Supplementary Note 4). By emulating neuronal threshold plasticity through chemical regulation, FON transduces chemical information into adaptive spiking, establishing a biomimetic framework for environmentally responsive iontronic computation.

## Discussion

In summary, we have experimentally demonstrated a spiking neuron analog using a polyelectrolyte-confined nanofluidic system under an asymmetric electrolyte environment. Leveraging the neuron-mimetic mechanism, the FON successfully emulates spiking behaviors in response to both electrical and chemical stimuli, producing oscillating ion currents with diverse patterns. The alternative ion conductance changes are regulated by the interdependent anion recognition/dissociation dynamics and EOF reversibility, effectively replicating key neural encoding features such as threshold responses, stimulus-dependent frequency modulation, and SFA. Furthermore, chemical regulation of the FON was achieved by modulating PimB-anion interactions, enabling precise control via ion species, concentration, and ionic strength to encode chemical information directly from the electrolyte. This programmability allowed us to simulate neuronal refractory-period threshold modulation by controlling $Fe(CN)_6^{3-}$ concentration gradient. Compared with conventional artificial spiking neurons that rely on complex memristor or transistor circuits, the FON emulates complex neuronal responses to multimodal signals within a single device, offering integrated encoding functionality alongside unparalleled structural simplicity (Supplementary Fig. 12).

https://doi.org/10.1038/s41467-025-66937-9

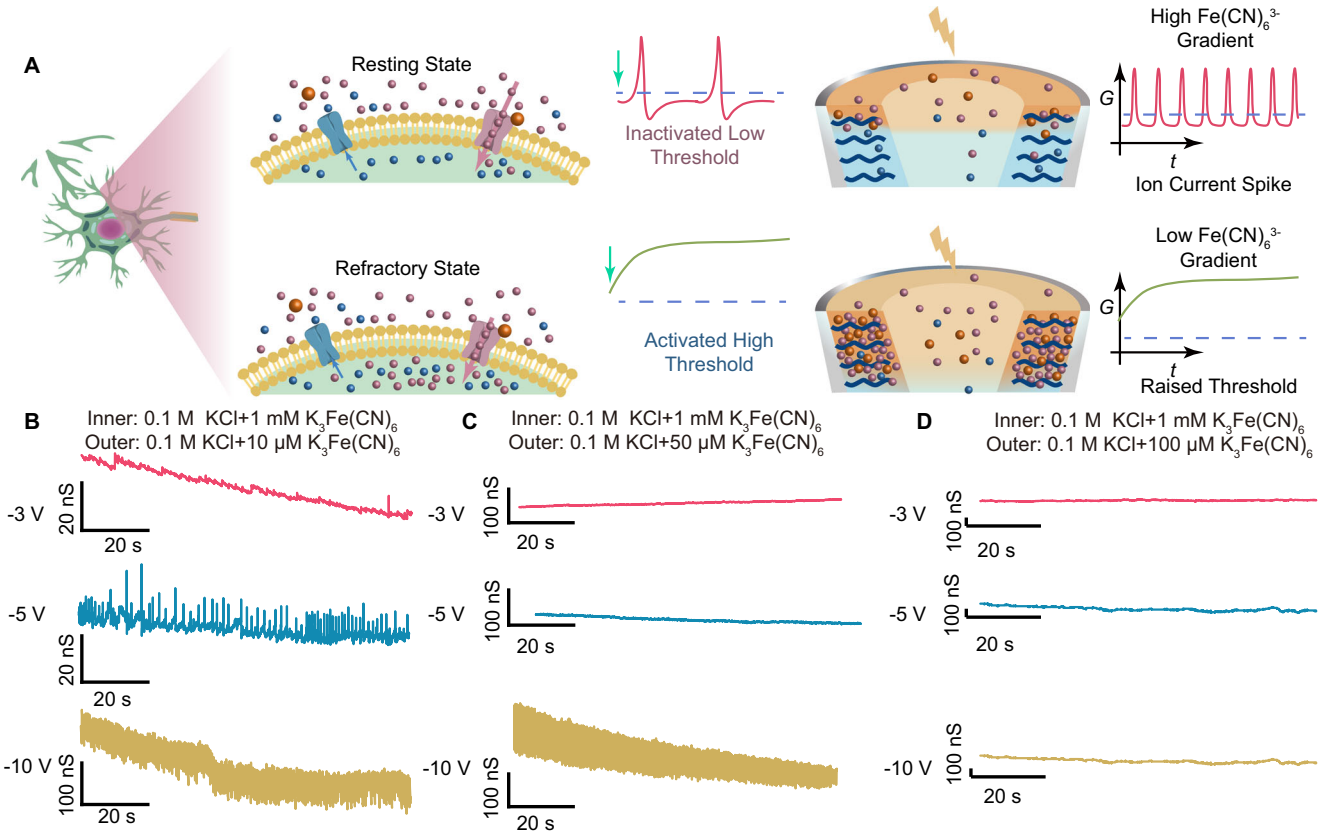


**Fig. 5 | Chemical regulated threshold shifts of FON. A** Schematic illustration on the low spiking threshold at resting state (upper) and high spiking threshold (lower) at refraction state of biological neurons (left) and FON (right). *G-t* curves of a FON in asymmetric solution with different concentration gradient and different biases (upper, −3 V; middle, −5 V; bottom, −10 V): **B** Inner: 0.1 M KCl+1 mM $K_3Fe(CN)_6$; Outer: 0.1 M KCl+10 μM $K_3Fe(CN)_6$; **C** Inner: 0.1 M KCl+1 mM $K_3Fe(CN)_6$; Outer: 0.1 M KCl+50 μM $K_3Fe(CN)_6$; **D** Inner: 0.1 M KCl+1 mM $K_3Fe(CN)_6$; Outer: 0.1 M KCl +100 μM $K_3Fe(CN)_6$.

The intrinsic advantages of fluidic systems—including chemical diversity, multi-ion flux synergies, and multimodal regulation—enable FON to achieve highly nonlinear spiking dynamics with a minimalistic architecture. This structural simplicity underpins their potential for neuron-mimetic computing and direct communication with biological systems. For instance, integrating FON devices into large-scale arrays could enable the realization of nanofluidic spiking neural networks that compute using ionic spikes. Similarly, interfacing FON devices with tissues or cells could establish intelligent biointerfaces capable of encoding external electrical and chemical signals into spiking ion currents for neuronal stimulation. While applications in these promising fields face challenges, such as limited spiking frequency and scalable integration strategies, future advances in sub-nanofluidic confinement and functionalized fluidic arrays may address these hurdles. Thus, FON represents a transformative platform for the development of adaptive, bio-inspired neuromorphic systems.

## Methods

### Synthesis of monomer and initiator

Synthesis of polyelectrolyte monomer 1-vinyl-3-butylimidazolium chloride [Vbim][Cl] and surface initiator 2-bromo-2-methyl-N-(3-(triethoxysilyl) propanamide) (BTPAm) were carried out following previous reported protocols[39,40]. [Vbim][Cl] monomer was synthesized by vigorously stirring the mixture of 1-vinylimidazole and 1-chlorobutane (1:3 molar ratio) under argon atmosphere in an oil bath of 70 °C for 75 h. The mixture was washed by ethyl acetate repeatedly to remove the unreacted 1-chlorobutane, and the top phase was decanted till the viscous liquid at the bottom was reversed to white solid. [Vbim][Cl] product could be obtained by finally filtering and drying the white solid at the bottom. The surface initiator BTPAm was synthesized by adding a 0 °C solution of 0.1 mL 2-Bromoisobutyryl bromide and 10 mL toluene to a cold mixture of 180 μL APTES, 120 μL TEA and 10 mL toluene dropwise at 0 °C under argon atmosphere. After constantly stir under 0 °C for 2 h and room temperature for 24 h, the mixture was filtered to remove the undissolved salts and further evaporated to get the yellow thick liquid BTPAm product.

### Fabrication of FON

FON devices were fabricated using SI-ATRP method following previous reported protocols[38,40]. Bare micropipettes were first fabricated by pulling pre-cleaned glass capillaries using a laser puller with parameters as follows:

(Line 1) Heat 405, Fil 5, Vel 25, Delay 28, Pull 10;

(Line 2) Heat 425, Fil 4, Vel 15, Delay 128, Pull 10.

The pore diameter and cone angle of the micropipettes were checked under an optical microscope to ensure the uniformity of the device. Hence, the micropipettes were backfilled with 5% BTPAm solution (in acetonitrile, v/v) and placed in an acetonitrile atmosphere overnight. By rinsed the micropipette with acetonitrile, ethanol and water 3 times respectively to remove the unreacted BTPAm, the initiator-modified micropipettes were prepared for further polymerization. ATRP reactions were carried out by backfilling and immersing the micropipette with a mixed solution of 50 mg·mL$^{-1}$ [Vbim][Cl] and 10 mg·mL$^{-1}$ N,N,N′,N″,N″-pentamethyldiethylenetriamine (PMDETA). ATRP were conducted by adding 35 mg CuBr to the external solution and heat under 65 °C oil bath for 24 h in an argon atmosphere. All solutions for ATRP were bubbled with argon for 20 mins to remove solved oxygen. After colling down to room

temperature, the modified micropipettes were thoroughly rinsed with deionized water till no $Cl^-$ existed.

### Synthesis and characterization of PimB-SiNPs

PimB-SiNPs were synthesized by following previous reported protocol[38], initially silica nanoparticles were first synthesized by adding 40 mL ammonium hydroxide (28–30%) into a flask containing 350 ml ethanol. 4 mL TEOS was added and the solution kept in a 20 °C water bath for 20 h under stir. By centrifuging the resulted milky suspension and carefully rinse the precipitation with ethanol and water, bare SiNPs were synthesized for further use. Prior to the SI-ATRP process, SiNPs were first activated by refluxing in 1 M HCl under 120 °C oil bath for 12 h, the activated SiNPs were carefully rinsed with water till the solution gets neutral. SI-ATRP was carried out by adapting the protocol for FON. i.e., first modify the nanoparticles with BTPAm and then carry out ATRP in a mixed solution of BTPAm-modified nanoparticle, CuBr, PMDETA and [Vbim][Cl] in a 65 °C oil bath under argon atmosphere. The modified PimB-SiNPs were further rinsed with water till no $Cl^-$ left. The zeta potential of the PimB-SiNPs in different solutions was measured with a ZEN 3600 Zetasizer (Malvern Instruments Ltd., UK).

### Characterization of FON

SEM images of the micropipettes were adopted with an S-4800 scanning electron microscope (Hitachi Inc., Japan). All electrical characterization experiments were performed on a Keithley 2636B Sourcemeter unit (Tektronix Co., U.S.A.) PimB-modified micropipettes were backfilled and immersed in electrolyte solutions with two Ag/AgCl wires placed in the micropipette and the external bath solution, respectively, to connect the circuit (Supplementary Fig. 1A). The potentials shown in the main text and supporting information were $V_{\mathrm{interval}}$ vs. $V_{\mathrm{external}}$. For the chemical regulation of FON, the devices were refreshed by backfilling and immersing the FON device in 1 M KCl solution for 30 min to remove the recognized $Fe(CN)_6^{3-}$ by the strong shielding effect of concentrated electrolyte. *G-t* curves in this communication were calculated based on the ion current and the applied bias voltages. Power spectra were derived from the *G-t* results with fast Fourier transform in OriginLab 2024 (OriginLab Corp.), and extended timescales were adopted for low-frequency spiking currents. The frequency information was adopted from the power spectra peak and the original *G-t* curves.

### FEM of EOF distribution in FON

FEM were carried out with COMSOL Multiphysics 6.3 (COMSOL Inc.) with a high-performance server (Lenovo Inc., China). Poisson equation, Nernst-Planck equation and modified Stokes-Brinkman Equation were numerically solved based on a steady-state 2D axial symmetric model (r,z). To describe the ion transport and EOF in FON under a constant $E = -3$ V bias voltage, the geometric model was described as follow: a conical micropipette with $r_0 = 5$ µm radius and $\theta = 3°$ half cone angle placed in a reservoir, the internal surface of the micropipette was modified with a uniform charge layer with thickness $d = 0.3$ µm (Supplementary Fig. 5). The detailed model was discussed in Supplementary Note 2.

## Data availability

All data needed to evaluate the conclusions in the paper are present in the main text or the supplementary materials. Source data are provided with this paper.

## References


1. Wu, F., Yu, P. & Mao, L. Neurotronics: communicating with brain through chemically intelligent materials. *Innov. Mater.* **1**, 100007 (2023).
2. Feng, J. et al. Single-layer $MoS_2$ nanopores as nanopower generators. *Nature* **536**, 197–200 (2016).
3. Yang, J. et al. Advancing osmotic power generation by covalent organic framework monolayer. *Nat. Nanotechnol.* **17**, 622–628 (2022).
4. Siria, A. et al. Giant osmotic energy conversion measured in a single transmembrane boron nitride nanotube. *Nature* **494**, 455–458 (2013).
5. Guo, G. et al. Hydrogel-filled micropipette enables antifouling in vivo iontronic sensing. *Sci. Bull.* **70**, 469–473 (2025).
6. Ahmed, S. A. et al. Iontronic sensing based on confined ion transport. *Anal. Chem.* **96**, 8056–8077 (2024).
7. Noy, A. & Darling, S. B. Nanofluidic computing makes a splash. *Science* **379**, 143–144 (2023).
8. Kamsma, T. M. et al. Brain-inspired computing with fluidic iontronic nanochannels. *Proc. Natl. Acad. Sci. USA.* **121**, e2320242121 (2024).
9. Emmerich, T. et al. Nanofluidics. *Nat. Rev. Methods. Primers* **4**, 69 (2024).
10. Noy, A., Li, Z. & Darling, S. B. Fluid learning: mimicking brain computing with neuromorphic nanofluidic devices. *Nano Today* **53**, 102043 (2023).
11. Maglia, G. et al. Droplet networks with incorporated protein diodes show collective properties. *Nat. Nanotechnol.* **4**, 437–440 (2009).
12. Liu, W. et al. Bioinspired carbon nanotube–based nanofluidic ionic transistor with ultrahigh switching capabilities for logic circuits. *Sci. Adv.* **10**, eadj7867 (2024).
13. Powell, M. R., Cleary, L., Davenport, M., Shea, K. J. & Siwy, Z. S. Electric-field-induced wetting and dewetting in single hydrophobic nanopores. *Nat. Nanotechnol.* **6**, 798–802 (2011).
14. Lu, J. et al. Efficient metal ion sieving in rectifying subnanochannels enabled by metal–organic frameworks. *Nat. Mater.* **19**, 767–774 (2020).
15. Tunuguntla, R. H., Allen, F. I., Kim, K., Belliveau, A. & Noy, A. Ultrafast proton transport in sub-1-nm diameter carbon nanotube porins. *Nat. Nanotechnol.* **11**, 639–644 (2016).
16. Lucas, R. A., Lin, C.-Y., Baker, L. A. & Siwy, Z. S. Ionic amplifying circuits inspired by electronics and biology. *Nat. Commun.* **11**, 1568 (2020).
17. Robin, P. et al. Long-term memory and synapse-like dynamics in two-dimensional nanofluidic channels. *Science* **379**, 161–167 (2023).
18. Xiong, T. et al. Neuromorphic functions with a polyelectrolyte-confined fluidic memristor. *Science* **379**, 156–161 (2023).
19. Emmerich, T. et al. Nanofluidic logic with mechano–ionic memristive switches. *Nat. Electron.* **7**, 271–278 (2024).
20. Zhang, P. et al. Nanochannel-based transport in an interfacial memristor can emulate the analog weight modulation of synapses. *Nano. Lett.* **19**, 4279–4286 (2019).
21. Xiong, T., Li, W., Yu, P. & Mao, L. Fluidic memristor: bringing chemistry to neuromorphic devices. *Innovation* **4**, 100435 (2023).
22. Xie, B. et al. Bioinspired ion-shuttling memristor with both neuromorphic functions and ion selectivity. *Proc. Natl. Acad. Sci. USA.* **122**, e2417040122 (2025).
23. Izhikevich, E. M. Which model to use for cortical spiking neurons? *IEEE Trans. Neural Netw.* **15**, 1063–1070 (2004).
24. Kumar, S., Williams, R. S. & Wang, Z. W. Third-order nanocircuit elements for neuromorphic engineering. *Nature* **585**, 518–523 (2020).
25. Mahowald, M. & Douglas, R. A silicon neuron. *Nature* **354**, 515–518 (1991).
26. Abu-Hassan, K. et al. Optimal solid-state neurons. *Nat. Commun.* **10**, 5309 (2019).
27. Harikesh, P. C. et al. Organic electrochemical neurons and synapses with ion-mediated spiking. *Nat. Commun.* **13**, 901 (2022).

28. Sarkar, T. et al. An organic artificial spiking neuron for in situ neuromorphic sensing and biointerfacing. *Nat. Electron.* **5**, 774–783 (2022).
29. Harikesh, P. C. et al. Ion-tunable antiambipolarity in mixed ion–electron conducting polymers enables biorealistic organic electrochemical neurons. *Nat. Mater.* **22**, 242–248 (2023).
30. Robin, P., Kavokine, N. & Bocquet, L. Modeling of emergent memory and voltage spiking in ionic transport through angstrom-scale slits. *Science* **373**, 687–691 (2021).
31. Kamsma, T. M., Boon, W. Q., ter Rele, T., Spitoni, C. & van Roij, R. Iontronic neuromorphic signaling with conical microfluidic memristors. *Phys. Rev. Lett.* **130**, 268401 (2023).
32. Bisquert, J. Iontronic nanopore model for artificial neurons: the requisites of spiking. *J. Phys. Chem. Lett.* **14**, 9027–9033 (2023).
33. Powell, M. R. et al. Nanoprecipitation-assisted ion current oscillations. *Nat. Nanotechnol.* **3**, 51–57 (2008).
34. Lee, C. Y., Choi, W., Han, J.-H. & Strano, M. S. Coherence resonance in a single-walled carbon nanotube ion channel. *Science* **329**, 1320–1324 (2010).
35. Wang, J. et al. Oscillatory reaction induced periodic C-quadruplex DNA gating of artificial ion channels. *ACS Nano* **11**, 3022–3029 (2017).
36. Deng, X. L., Takami, T., Son, J. W., Kawai, T. & Park, B. H. Ion current oscillation in glass nanopipettes. *J. Phys. Chem. C.* **116**, 14857–14862 (2012).
37. Hodgkin, A. L. & Huxley, A. F. A quantitative description of membrane current and its application to conduction and excitation in nerve. *J. Physiol.* **117**, 500–544 (1952).
38. He, X. et al. Micrometer-scale ion current rectification at polyelectrolyte brush-modified micropipets. *J. Am. Chem. Soc.* **139**, 1396–1399 (2017).
39. Zhao, F., Meng, Y. J. & Anderson, J. L. Polymeric ionic liquids as selective coatings for the extraction of esters using solid-phase microextraction. *J. Chromatogr. A* **1208**, 1–9 (2008).
40. Rutnakornpituk, M., Puangsin, N., Theamdee, P., Rutnakornpituk, B. & Wichai, U. Poly(acrylic acid)-grafted magnetic nanoparticle for conjugation with folic acid. *Polymer* **52**, 987–995 (2011).
41. Powell, M. R., Vlassiouk, I., Martens, C. & Siwy, Z. S. Nonequilibrium *1/f* noise in rectifying nanopores. *Phys. Rev. Lett.* **103**, 248104 (2009).
42. Gravelle, S., Netz, R. R. & Bocquet, L. Adsorption kinetics in open nanopores as a source of low-frequency noise. *Nano Lett.* **19**, 7265–7272 (2019).
43. Yu, P., He, X., Zhang, L. & Mao, L. Dual recognition unit strategy improves the specificity of the adenosine triphosphate (ATP) aptamer biosensor for cerebral ATP assay. *Anal. Chem.* **87**, 1373–1380 (2015).
44. Zhuang, X. et al. Strong interaction between imidazolium-based polycationic polymer and ferricyanide: toward redox potential regulation for selective in vivo electrochemical measurements. *Anal. Chem.* **84**, 1900–1906 (2012).
45. He, X. et al. Chaotropic monovalent anion-induced rectification inversion at nanopipettes modified by polyimidazolium brushes. *Angew. Chem. Int. Ed.* **57**, 4590–4593 (2018).
46. Bocquet, L. & Charlaix, E. Nanofluidics, from bulk to interfaces. *Chem. Soc. Rev.* **39**, 1073–1095 (2010).
47. Lan, W.-J. et al. Voltage-rectified current and fluid flow in conical nanopores. *Acc. Chem. Res.* **49**, 2605–2613 (2016).
48. Wu, X., Ramiah Rajasekaran, P. & Martin, C. R. An alternating current electroosmotic pump based on conical nanopore membranes. *ACS Nano* **10**, 4637–4643 (2016).
49. Luo, L., Holden, D. A. & White, H. S. Negative differential electrolyte resistance in a solid-state nanopore resulting from electroosmotic flow bistability. *ACS Nano* **8**, 3023–3030 (2014).
50. Yusko, E. C., An, R. & Mayer, M. Electroosmotic flow can generate ion current rectification in nano- and micropores. *ACS Nano* **4**, 477–487 (2010).
51. Yang, R. et al. Negative differential resistance in conical nanopore iontronic memristors. *J. Am. Chem. Soc.* **146**, 13183–13190 (2024).
52. White, H. S. & Bund, A. Ion current rectification at nanopores in glass membranes. *Langmuir* **24**, 2212–2218 (2008).
53. Hyland, B., Siwy, Z. S. & Martens, C. C. Nanopore current oscillations: nonlinear dynamics on the nanoscale. *J. Phys. Chem. Lett.* **6**, 1800–1806 (2015).
54. Connors, B. W. & Gutnick, M. J. Intrinsic firing patterns of diverse neocortical neurons. *Trends Neurosci.* **13**, 99–104 (1990).
55. Bi, G. & Poo, M. Synaptic modifications in cultured hippocampal neurons: dependence on spike timing, synaptic strength, and postsynaptic cell type. *J. Neurosci.* **18**, 10464–10472 (1998).
56. Hodgkin, A. L. The local electric changes associated with repetitive action in a non-medullated axon. *J. Physiol.* **107**, 165–181 (1948).
57. Benda, J. & Herz, A. V. M. A universal model for spike-frequency adaptation. *Neural Comput.* **15**, 2523–2564 (2003).
58. McDonnell, M. D. & Ward, L. M. The benefits of noise in neural systems: bridging theory and experiment. *Nat. Rev. Neurosci.* **12**, 415–425 (2011).
59. Gammaitoni, L., Hänggi, P., Jung, P. & Marchesoni, F. Stochastic resonance. *Rev. Mod. Phys.* **70**, 223–287 (1998).


## Acknowledgements

This work is supported by the National Natural Science Foundation of China (22504156 for T.X., 22125406, 22550002 and T2596021 for P.Y., 22134002 and T2596020 for L.M., 22304011 for C.P. and 22574162 for W.M.), the Natural Science Foundation of Beijing (F251009 and Z230022 for P.Y., 2242028 for W.M.), the National Basic Research Program of China (2022YFA1204500 for P.Y., 2022YFA1204503 for P.Y. and 2024YFA1803403 for L.M.) and China Postdoctoral Science Foundation (BX20240381, 2025M771067 for T.X.).

## Author contributions

P.Y. and L.M. conceived the idea, supervised this work and got funding for the research; T.X., X.H., F.W., W.M., Y.J., P.Y., and L.M. designed the methodology; T.X., X.H., B.X., G.G., H.Z., Y.L., and C.P. investigated the performance and mechanism of the device. T.X., X.H., B.X., G.G., H.Z., Y.L., C.P., F.W., W.M., and Y.J. visualized the results. T.X., X.H., and P.Y. wrote the manuscript; T.X., P.Y., and L.M. revised and finalized it. All authors contributed comments on this work.

## Competing interests

The authors declare no competing interests.

## Additional information

**Supplementary information** The online version contains supplementary material available at https://doi.org/10.1038/s41467-025-66937-9.

**Correspondence** and requests for materials should be addressed to Ping Yu or Lanqun Mao.

**Peer review information** *Nature Communications* thanks the anonymous reviewers for their contribution to the peer review of this work. A peer review file is available.

**Reprints and permissions information** is available at http://www.nature.com/reprints

**Publisher's note** Springer Nature remains neutral with regard to jurisdictional claims in published maps and institutional affiliations.

**Open Access** This article is licensed under a Creative Commons Attribution-NonCommercial-NoDerivatives 4.0 International License, which permits any non-commercial use, sharing, distribution and reproduction in any medium or format, as long as you give appropriate credit to the original author(s) and the source, provide a link to the Creative Commons licence, and indicate if you modified the licensed material. You do not have permission under this licence to share adapted material derived from this article or parts of it. The images or other third party material in this article are included in the article's Creative Commons licence, unless indicated otherwise in a credit line to the material. If material is not included in the article's Creative Commons licence and your intended use is not permitted by statutory regulation or exceeds the permitted use, you will need to obtain permission directly from the copyright holder. To view a copy of this licence, visit http://creativecommons.org/licenses/by-nc-nd/4.0/.

© The Author(s) 2025